Ecotoxicology and Environmental Safety 293 (2025) 118040

Contents lists available at ScienceDirect

Ecotoxicology and Environmental Safety

journal homepage: www.elsevier.com/locate/ecoenv

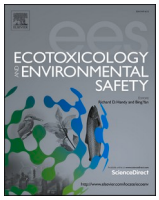

Transcriptomic and metabolic profiling reveals the effects of long-term microwave exposure on testicular tissue

Binwei Yao [a,1], Jing Zeng [b,1], Jingqi Shi [c,1], Yueyue Pang [a,d], Junqi Men [a], Yanyang Li [a], Heran Wang [c], Jing Liu [c], Wang Hui [a], Li Zhao [a], Chunlin Li [b,*], Ruiyun Peng [a,*], Jiao Fan [c,*]

[a] Beijing Institute of Radiation Medicine, Beijing 100850, China
[b] Department of Endocrinology, National Clinical Research Center of Geriatrics Disease, Second Medical Center of Chinese PLA General Hospital, National Key Laboratory of Kidney Disease, Beijing 100853, China
[c] Institute of Geriatrics, National Clinical Research Center of Geriatrics Disease, Second Medical Center of Chinese PLA General Hospital, Beijing 100853, China
[d] College of Chemistry and Materials Sciences, Hebei University, Baoding 071002, China

ARTICLE INFO

Edited by Mohamed Abdel-Daim

Keywords:
Single-cell assays for transposase-accessible chromatin sequencing
Single-cell RNA sequencing
Long-term pulsed microwave exposure
Reproductive damage
Germ cell differentiation

ABSTRACT

The effect of electromagnetic exposure on health is becoming increasingly important as it affects many aspects of human life and health. However, the effects in environmental electromagnetic fields on the male reproductive system were still controversial, and the impacts of long-term microwave exposure on testicular tissue remain poorly defined. This study exposed rats to 30 mW/cm^2 of microwave radiation (2.856 GHz) for six weeks and revealed that long-term microwave exposure damaged the testis structures, sperm motility, and morphology, affected hormone levels, energy metabolism, and induced oxidative stress. Assays for bulk RNA, metabonomics, single-cell RNA, and transposase-accessible chromatin with high-throughput sequencing were performed to analyze the transcriptional and metabolic atlas of testicular damage after microwave radiation. Differentially expressed genes were enriched in oxidative stress and energy metabolism pathways. Furthermore, ten subgroups were identified with scRNA-seq, including five developmental phases of germ cells, and radiation-associated changes in cell composition, especially stuck in round spermatids, were observed. Radiation significantly upregulated the expression of Atp6v1e2 in round spermatids and enriched the expression of many transcription factors by disturbing the accessibility profile of chromatin. This study provides effective insights into the long-term impacts of microwave radiation on male reproduction.

1. Introduction

With the widespread application of electromagnetic technology in military, communication, transportation, medical, and other fields, exposure to radiofrequency electromagnetic fields (100 KHz-300 GHz) has been increasing, which have been listed by the World Health Organization as the fourth major source of pollution after water, noise and air pollution. The negative health effects of electromagnetic exposure, particularly in the S-band (2–4 GHz), the most widely used in the microwave frequency range (300 MHz-300 GHZ), have gradually become a topic of global concern (Belpomme et al., 2018; Verbeek et al., 2021). The S-band was broadly applied in civil communication fields, including mobile phones (Hasan et al., 2022; Yu et al., 2020), WiFi (Shokri et al., 2015), base station antennas (Balmori, 2022), and occupational exposure scenes such as radar systems (Peleg et al., 2023). Those working in communication base stations and radar systems and residents living in the vicinity have a high probability of being exposed to microwave radiation for a long time. Microwave exposure affects multiple organ systems and can affect sleep (Liu et al., 2021), cause cognitive impairment (Hao et al., 2023), reduce immunity (Yao et al., 2023) and cardiomyocyte damage (Wang et al., 2018), and even increase the risk of certain cancers (Peleg et al., 2023).

Testes containing spermatogenic cells are highly sensitive to microwave radiation as they exhibit a weaker protective effect on tissues and are more easily penetrated by microwaves (Houston et al., 2016). Microwave exposure at certain levels may lead to spermatogenic cell damage, interstitial edema, decreased sperm motility, and abnormal gonadal hormone secretion in testicular tissues (Jaffar et al., 2019;

* Corresponding authors.
E-mail addresses: lichunlin301@163.com (C. Li), ruiyunpeng18@126.com (R. Peng), fanjiao@301hospital.com.cn (J. Fan).
[1] Binwei Yao, Jing Zeng, and Jingqi Shi contributed equally.

https://doi.org/10.1016/j.ecoenv.2025.118040
Received 18 March 2024; Received in revised form 17 February 2025; Accepted 9 March 2025
Available online 13 March 2025

Vornoli et al., 2019; Yu et al., 2020). To date, previous findings regarding the effects of microwave exposure on male reproduction remain controversial, particularly regarding pulsed microwave exposure (Pacchierotti et al., 2021). This is largely because of differences in the duration and degree of exposure, multiple testing methods and inconsistencies among experimental models (Bernabò et al., 2017).

Additionally, many traditional experiment methods have been performed to explore the reproductive damage from radiation, with the disadvantages of lacking resolution at cell-to-cell heterogeneity or concentration on a narrowly defined set of factors (Lukassen et al., 2018; La et al., 2021). Recently, the regulation of testis cell development in mice, macaques, and humans has been analyzed previously using scRNA-seq (Guo et al., 2018; Hermann et al., 2018; Shami et al., 2020), which can identify cell specificity and explore rare and scarce target cells. Although much is already known about spermatogonia and the differentiation process, less is known about the testis damage and changes in cell components and signaling pathways after radiation. Moreover, the integrative analysis of mRNA expression and chromatin accessibility in testicular cells of rats has not been investigated at the single-cell level. This study performed assays for bulk RNA, metabonomics, scRNA-seq, and scATAC-seq with high-throughput sequencing to explore the transcriptional single-cell and metabolic atlas of rat testis after long-term microwave radiation and identify the cell-specific genes, chromatin accessibility markers and gene regulatory network of each cell type. This study provides a comprehensive analysis of the effects of microwave exposure on rat testis tissue at transcriptional and metabolic levels, as well as potential insights and targets for the protection and treatment of microwave radiation injury in human populations with occupational exposure.

2. Materials and methods

2.1. Animals

Twenty Wistar male rats (six to eight weeks old; 200 ± 20 g) were obtained from Vital River Laboratory Animal Technology Co., Ltd. (Beijing, China). Standard food and water were provided for all rats. Then, rats were randomly divided into control and irradiation groups. This study was approved by the Institutional Animal Care and Use Committee (IACUC-AMMS-2020–780). And animals were handled following the US National Institutes of Health Guide for the Care and Use of Laboratory Animals.

2.2. Microwave exposure

Rats were fixed in plastic boxes with vent holes and placed under a horn antenna in a specific direction for radiation. The irradiation group was exposed to a 2.856-GHz high-power microwave field, located in the frequency band of S-band, for 15 min/day for six weeks. Control rats received the same conditions as the radiation group but were not exposed to microwaves. The radiation system included a microwave generator, an antechamber, and a control unit. Energy transmission depended on an A10-dB standard-gain antenna and a rectangular waveguide. The distance between the antenna and cage top was 0.9 m, and microwave pulses were transmitted with a pulse width of 600 pps, a pulse width of 500 ns for irradiation, and a peak power density of 100 W/cm^2. Power meters (Agilent N1912, N1921) were used to monitor the forward power of the transmission received from a directional coupler at 900 kW. The average power density of the exposed group was 30 mW/cm^2, considering its reported damages on hippocampal neurons (Hao et al., 2022), natural killer cells (Zhao et al., 2017) et al., and previous finding from our laboratory (Men et al., 2023). The average specific absorption ratio (SAR) of testicular tissues and the whole body was calculated and based on the finite-difference time--domain method using the software package Sim4life v6.0 (ZMT, Zurich, Switzerland). The formula is SAR $= \sigma E^2/\rho$ (W/kg), where E stands for the electric field strength (V/m), σ (sigma) stands for the electrical conductivity (S/m), and ρ (rho) stands for the sample density (kg/m^3). The average SAR values of the whole body and testicular tissue in the exposed groups were 9 W/kg and 19.8 W/kg, respectively. To clarify temperature changes during the exposure process, the anal temperature of six rats was recorded in real-time by an optical fiber during the exposure process. The temperature of the exposure group averaged 0.83 ℃, which was higher than that of the control group.

2.3. Sperm motility test

A computer-assisted semen analysis system (Hamilton Thorne, USA)-TOX IVOS II™ CASA System was used to assess sperm motility. Sperm were collected and evaluated; at least 1000 sperm were collected per sample. The sperm motility rating was divided into four levels: (1) Grade A, rapid progressive sperm; (2) Grade B, sluggish progressive sperm; (3) Grade C, nonprogressive sperm; and (4) Grade D, immotile sperm.

2.4. Sperm morphology analysis

Pre-stained slides morphology analysis sperm blue (Art. no. GC-SB-100, Golgcyto, Guangzhou, China) and SCA® CASA System for semen (Golgcyto, Guangzhou, China) were used to analyze sperm morphology. The parameters used to observe sperm morphology included arc, head width, head area, head circumference, linearity, angle, degree of head fold, midpiece width, and midpiece insertion angle.

2.5. Sperm DNA integrity measurement

We used the halosperm sperm DNA fragmentation detection kit (HT-HS10, Halotech DNA SL, Madrid, España) to assess DNA fragmentation. The sperm were mixed with agarose gel and dropped onto the pretreated slide. A denaturation solution was used to treat glass slides and denature the DNA of these sperm cells. Then, the sample was treated with a lysis solution, which breaks the cellular membrane, removing most of the nuclear proteins. Then, the prepared glass slides were observed by the SCA® CASA System for semen (Golgcyto, Guangzhou, China). Big halos appear around the head of the sperm cell, which would be observed without damage to the DNA. Those sperm cells with fragmented DNA would show small or absent halos.

2.6. Biochemical analysis

After anesthesia, the serum was prepared by collecting blood from the main abdominal vein. Insulin-like factor 3, inhibin-B (INHB), testosterone (T), luteinizing hormone (LH), and follicle-stimulating hormone (FSH) levels were evaluated using the radioimmunoassay (XH6080, Xi'an Nuclear Instrument Co., Ltd., China) and sensitive immunoradiometric assay with commercial kits (Beijing Furui Runze Biotechnology Co., Ltd., China).

Testes were split in a lysis buffer and centrifuged at 4 ℃. Then, the supernatants were gathered to estimate the contents of lactate dehydrogenase (LDH), succinic dehydrogenase (SDH), and adenosine triphosphate (ATP) synthase with assay kits following the manufacturer's instructions (Jianglai Biotechnology Co., Ltd., Shanghai, China). The enzyme-linked immunosorbent assay (Rayto, RT-6100, USA) was used to measure absorbance. Malondialdehyde (MDA) concentrations and superoxide dismutase (SOD) activity were estimated with commercial kits (19160; MAK085; SIGMA, USA). The absorbance of the oxidative product or antioxidant enzyme was determined using a spectrometer.

2.7. Hematoxylin–eosin staining

The testes were fixed in a 10 % neutral formalin buffer for at least one week and then embedded in paraffin. Next, 3-μm testicular sections were

dyed with hematoxylin-eosin (Sinopharm Chemical Reagent Beijing Co., Ltd.). Clearance of xylene and coverslips was performed after gradient ethanol dehydration. Observations were performed with a LEICA DM6000 light microscope (Leica, Germany).

2.8. Ultrastructure of testicular tissue

All testicular tissues were gathered and then fastened in the 2.5 % glutaraldehyde. Tissues were incubated with 1 % osmium tetroxide and gradient ethyl alcohol, then embedded in EPON618 (TAAB Laboratories Equipment, Berks, UK). Staining was performed using lead citrate and uranyl acetate (Advanced Technology & Industrial Co. Ltd., Hong Kong, China). Transmission electron microscopy (H-7800, Tokyo, Japan) was used to visualize the slides.

2.9. Bulk RNA-seq data collection, quality control, processing, and functional annotation analysis

Total RNA samples of testicular tissues from three irradiated and three control rats were isolated with TRIzol reagent (Invitrogen). An RNA-seq sequencing library was built according to Illumina's standard protocols, and the RNA quality was determined with an Agilent 2100 Bioanalyzer. Sequencing data were created using the Illumina HiSeq platform of Novogene with a 150-bp paired-end read length. After quality control with FastQC (v0.11.8), Trim Galore (v0.6.1) was performed to remove low-quality reads and adaptors. We used default parameters to compare the trimmed RNA-seq data with the *Rattus norvegicus* transcriptome in STAR (v2.5.0a). Gene expression was quantified by HTSeq (v0.10.0). DESeq2 (V1.40.1) was applied to explore the differentially expressed genes (DEGs), defined as fold changes of the expression were > 1.5 or < 0.67, and the *P*-value was < 0.05. ClusterProfiler package was used to complete the gene set enrichment analysis (GSEA) (Subramanian et al., 2005). Enrichment analysis with Gene Ontology (GO) and Kyoto Encyclopedia of Genes and Genomes (KEGG) were performed for DEGs of testicular tissue through the DAVID online software. The biological processes and pathways were considered enriched at $P < 0.05$.

2.10. Untargeted metabolomics analysis

Tissues from five control and five irradiated rat testis tissues were prepared by grinding 100 mg of each in liquid nitrogen and then adding 500 μL of 80 % methanol to the resulting powder in EP tubes. After vortexing and chilling on ice for 5 min, the mixtures were centrifuged at 15,000 g for 20 min at 4℃. Supernatants were collected and diluted with mass-spectrometry-grade water to reduce the methanol concentration to 53 %, followed by another centrifugation at 15,000 g for 20 min at 4℃. The clarified supernatants were transferred to EP tubes for analysis. The prepared samples were then subjected to chromatographic and mass spectrometric analysis using a Vanquish UHPLC system coupled with a Q ExactiveTM HF-X mass spectrometer (Thermo Fisher, Germany) in both positive (ESI^+) and negative (ESI^-) ion modes. Chromatographic separation was performed on a HypersilGold column (C18) with a gradient elution system comprising water with 0.1 % formic acid (solvent A) and methanol (solvent B). The mass spectrometer operated in full-scan mode, acquiring data across a mass range of 100–1500 *m/z*. The raw files obtained from mass spectrometry detection were imported into Compound Discoverer 3.3 software and combined with a high-quality mzCloud database constructed from standard samples, along with mzVault and MassList databases, to match and identify molecular characteristic peaks, obtaining qualitative and quantitative results of metabolites. Differentially expressed metabolites (DEMs) were screened based on the criteria of VIP > 1.0, FC > 1.2 or FC < 0.833, and *P*-value < 0.05.

2.11. Sample preparation for single-cell RNA sequencing

After surgical removal, the testicular tissues of rats were cut into small pieces. Tissues were cleaned twice with phosphate-buffered saline (PBS) and digested into a single-cell suspension. As for single-cell scale data, cellular suspensions from irradiated and control samples were diluted to 1×10^6 cells/mL for further analysis. Then, the barcoded cDNA library for each cell in the suspension was generated on the 10X Genomics platform. Bioanalyzer (Agilent) was used to estimate the data quality, and the KAPA Library Quantification Kit (Roche) was used for quantification. Then, all libraries were merged for sequencing on the HiSeq 2500 platform (Illumina).

2.12. ScRNA-seq quantification and data analysis

CellRanger was used to implement gene quantification and generate gene barcode matrices, with *Rattus norvegicus* (mRatBN7.2) as the reference genome. Seurat R package (V4.1.1) was used for downstream analysis. A Seurat object was created with the count matrix, and quality control, normalization, and scaling were subsequently performed (Stuart et al., 2019). Poor-quality cells were filtered out using the following criteria: $>$ 400 unique feature counts, $>$ 0.5 % hemoglobin counts, and $>$ 5 % mitochondrial counts, leaving 11,848 control and 11,536 irradiated cells for analysis. Qualified cells were normalized using the "LogNormalize" method, and genes with high variability were explored by the FindVariableFeatures function. By default, each dataset returned 2000 features. Linear transformation and dimensional reduction were implemented sequentially using ScaleData and principal component analysis. Then, JackStrawPlot was used to assess the "dimensionality" of the Seurat object, and the top 12 components were chosen and further visualized by uniform manifold approximation and projection (UMAP). The FindClusters function performed cell-type clustering with a resolution of 0.04, resulting in 10 distinct clusters. Finally, the FindMarkers function was used to identify the DEGs between different cell clusters.

2.13. ScATAC-seq quantification and data processing

The scATAC-seq library was also prepared using the 10X Genomics platform as recommended. The FastQ file was transformed from the raw sequencing data by the "CellRanger-ATAC mkfastq" pipeline. ScATAC-seq reads were matched and quantified using the "CellRanger-count" pipeline, with *Rattus norvegicus* (mRatBN7.2) as the reference genome. Signac (v1.5) was used for downstream analyses, including integration of the irradiated and control datasets, UMAP dimensionality reduction, identification of cell clusters and differentially accessible regions, and integration of scATAC-seq and scRNA-seq data by transferring labels from the scRNA-seq dataset. Dimensionality reduction was performed using a latent semantic index. Concrete parameters involved min.dist $= 0.5$ for "RunMAP" and resolution $= 0.08$ for "FindCluster".

We used the CoveragePlot function to simultaneously visualize gene expression and DNA accessibility information, to compare DNA accessibility in each region for different cell types, and to cover gene expression information for different genes. The JASPAR2020 motif model was used for DNA motif scanning. ChromVAR (version 1.12.0) was used to analyze motif accessibility in the merged scATAC-seq peaks. We then used "Findmarkers" to explore the over-represented DNA motifs in a set of peaks, with differential accessibility between cell types, to explore potentially important cell-type-specific sequences. Two conditions were set for identifying differential ATAC-seq peaks between irradiated and control groups: at least 0.25 % cells with non-zero signals in any cluster and $P < 0.05$.

2.14. Analysis of cell-cell communications

CellChat was performed to identify the cell-cell communication and

ligand-receptor interaction in the scRNA-seq data, with $P < 0.05$ indicating a significant difference (Jin et al., 2021).

2.15. Fluorescence in situ hybridization (FISH)

Testicular tissue was removed and immediately fixed in 4 % paraformaldehyde. After fixation, the testicular tissue underwent a treatment process of dehydration, wax immersion, and embedding. The paraffin section was removed with a spreader, baked in an oven at 62 ℃ for 2 h, dewaxed to water, and washed with xylene I, then xylene II for 15 min. The section was washed with absolute ethanol I and II, 85 % ethanol, and 75 % ethanol for 5 min, and finally washed with diethylpyrocarbonate-treated water. Sections were then boiled in retrieval buffers and cooled naturally, managed by adding proteinase K dropwise with a concentration of 20 μg/mL at 37 ℃, flushed with pure water, and cleaned with PBS three times for 5 min. After pre-hybridization and incubation at 37 ℃ for 1 h, the probe containing the hybridization solution was added dropwise and then incubated at 40 ℃ overnight. Next, different saline sodium citrate buffer dilutions were used to wash the hybridization solution the following day. Blocking serum (bovine serum albumin) was then added dropwise and the mixture was blocked for 30 min at room temperature. The blocking solution was decanted, anti-DIG-488 was added dropwise, and the mixture was incubated at 37 ℃ for 50 min, followed by abstersion with PBS four times for 5 min. Finally, sections were stained with 4', 6-diamidino-2-phenylindole (DAPI) to counterstain nuclei, incubated in the dark for 8 min, flushed, and mixed with an anti-fluorescence quenching sealing agent. Finally, a fluorescent microscope was used for observation and image acquisition (Nikon, Japan). Table 1 shows the probe sequences used in this study.

Table 1
Sequences of FISH probes used in this study.

Probe name	Sequence
Dazl	AAATCCATAGCCCTTCGACACACC, GTTTCATCCATCCTAACATCAATTCCA, CATGATAAGTACATAAATTTTGTTTCCTG, GAGGATATGCCTGAACATACTGAGTG, AGATTTCTTTTGTGGGCCATTTCC
Spaca1	TTTGTTCTGAACCTCTTCCTCGGC TGATACCAACACCACACGTGACTGT GTCTACCCCAGCCACAATCAACAG ATAACAGGTTGTTGATCTGGCTTTAG ACTGCCGCCCAATTTATGATTATG
Rpl4	AACAAAGTTCACAATATCCGGTCGA GCATAGGGCTGTCTATTGTTCTTCC CCTCCTTGGTCTTCTTATAACTTTCA
Camk4	CCCACCAGGGGGAGATAAAGTAA AATGTAGTCAGCCGCTTCTTAGGGT AAGTTGGCTGCTTTTCCTGTGACC GTGTGACTGCTGCTGGCACTTC CGAGCTGGCTTTGTTGCTTTCTT ATCTGTCTTGTCCTTGCCGTCTTG TCGGACTGTAGCTTCATCGTCTCAT
Atp6v1e2	GTCTATCTCCTCCGCCTTCTCATT ATCTTCGCCTCTTTGAGCAGTTCC TCTTGGTAGAACTCTTCATCCGACA GTTCTCTGCATCGGACAATCATCAC CAGCATTGGAAGACAAGTATTCAGTTT ATTTTCCGATCGCTGCTATAGACCT
Spaca7	ATTCAGTCGGCTTTCTAGGGTATTG CAGCAGGAAAACGGATAAGAAGGTC GAAGTTGTCTTGACTGGATGTAGCTC AGGTTTCAGGTATGTTTTCAGTTGTT TGAAGTTCTTGGCTCCAAAATATCT CAGCATTTGGTTCCTTGGTTTGTA GTTCTCAAAGGCTTCCTCTTGGTAG TGATAGACTTGCTTTCCGGATACAG TGTATTGTACGTTTGCGATTTCTAGTC

2.16. Statistical analysis

R 4.0.5 software was employed for statistical analysis. The Wilcoxon rank-sum test was used to estimate the difference of DEGs between groups in the violin plots. $P < 0.05$ was considered statistically significant.

3. Results

3.1. Long-term microwave exposure directly impaired testes

To explore the impact of long-term microwave exposure on male reproductive organs, we exposed male rats to 2.856-GHz microwave radiation for six weeks, with an average power density of 30 mW/cm^2, a pulse width of 500 ns, and an average SAR of 19.8 W/kg. Compared to the control group, the rectal temperature in the irradiation group increased by an average of 0.83 ℃ (Fig. 1A-C). According to radioimmunoassay results, the levels of INHB, LH, and FSH were decreased in microwave-exposed rats, whereas IGF-3 levels were increased (Fig. 1D). Changes in these indicators suggested that microwave exposure caused hormonal disorders, thereby affecting reproductive health. The decrease in sperm DNA integrity showed sperm DNA damage after microwave exposure (Fig. 1E). In addition, there was a significant reduction in the proportion of Grade AR and Grade A+B spermatozoa, alongside an elevation in the Grade D spermatozoa, suggesting that microwave exposure has an adverse impact on the viability of sperm in male rats (Fig. 1F). The arc, angle, and midpiece insertion angle of sperm were reduced. The head width, head area, head circumference, linearity, degree of head fold, and midpiece width were elevated in sperm (Fig. 1G). Changes in these parameters indicated abnormal sperm morphology after microwave exposure. After microwave exposure, the SOD activity decreased, the MDA level increased, and the LDH, SDH, and ATP synthase levels decreased (Fig. 1H-I), indicating that testicular injury induced by microwave exposure was related to oxidative stress and energy metabolism disorders in rats. Hematoxylin—eosin staining showed that testicular spermatogenic cells were disordered and swollen after microwave exposure, vacuoles formed, and interstitial edema was observed (Fig. 1J). Ultrastructural analysis showed that the chromatin of mesenchymal cells was abnormally condensed and shifted to the side, some mitochondrial cristae disappeared, and the endoplasmic reticulum was vacuolated after microwave irradiation. The spermatogonia and spermatocytes were swollen, and the mitochondria were vacuolated. The round spermatids showed the swelling and vacuolation of mitochondria and unclear nuclear membranes, and the spermatids had uneven chromatin distribution (Fig. 1K-N). The results indicated that long-term microwave exposure affects reproductive function and structure in male rats, with oxidative stress and energy metabolism playing an important role.

3.2. Characteristics of DEGs in testicular tissues receiving microwave radiation

Bulk RNA sequencing was performed to determine the comprehensive transcriptome profile of testicular tissues with radiation. The correlation heatmap illustrated the relationship between each dataset and the other datasets (Fig. 2A). A total of 42,277 genes were observed in the irradiated rats, of which 226 were upregulated, and 256 were downregulated (Fig. 2B-C; Table S1). Cebpb, which encodes the important transcription factor CCAAT/enhancer binding protein β (C/EBPβ), was significantly upregulated among them. Long-term microwave exposure also upregulated the levels of Gpx5, which is related to oxidative stress and spermatogenesis (Maremanda et al., 2016), and CFTR, which is a potential target for post-meiotic fertility regulation (Sharma et al., 2018).

To better understand the biological functions of DEGs induced by long-term high-power pulsed microwave radiation, we used GSEA to

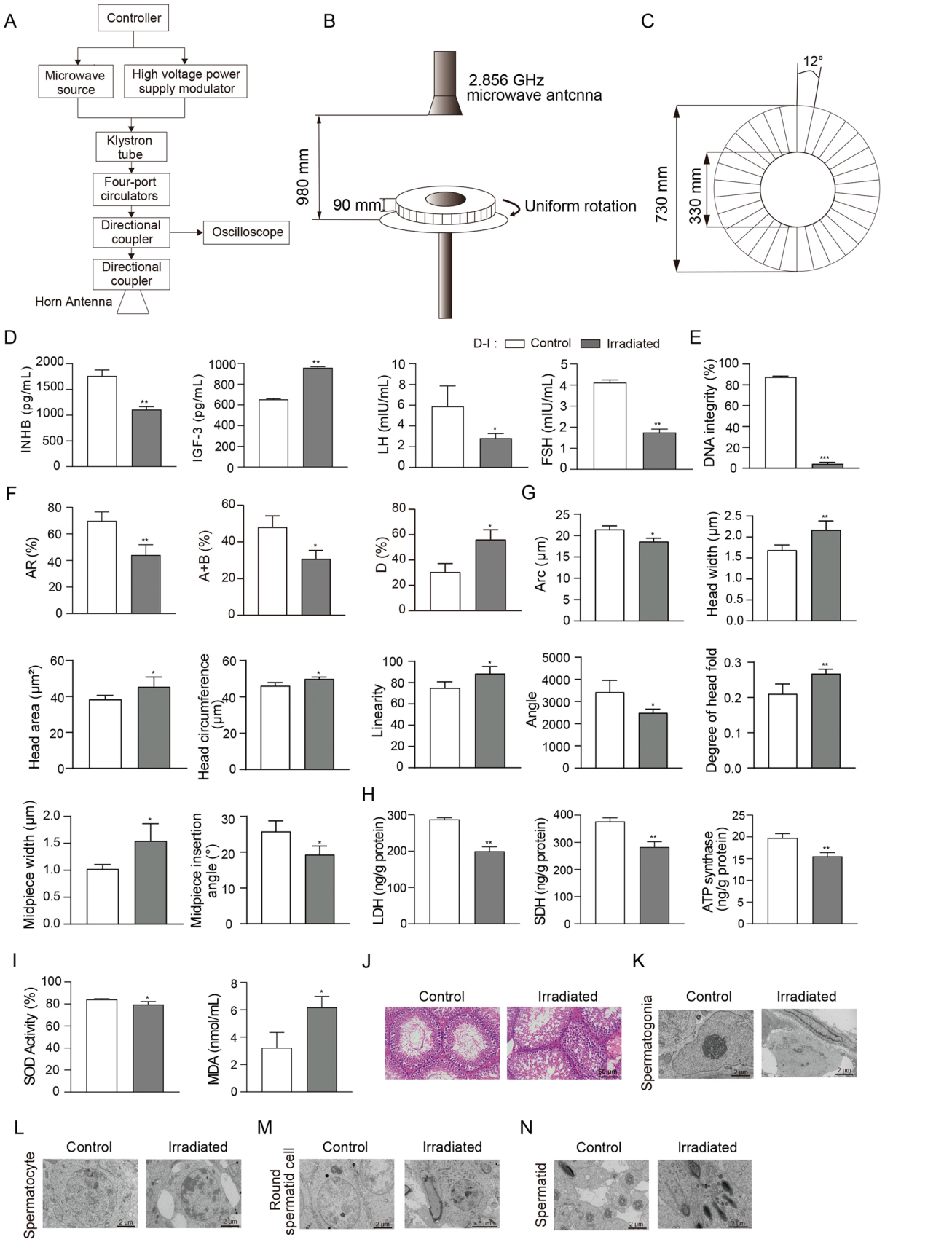

(caption on next page)

Fig. 1. Microwave exposure model and changes in hormone levels, sperm quality, testicular tissue structure, the indexes of oxidative stress, and energy metabolism enzyme in rats after microwave radiation. Schematic diagrams of (A) the microwave radiation source, (B) the microwave radiation process, and (C) the rat container. (D) Levels of serum hormone inhibitor B (INHB), insulin-like factor 3 (IGF-3), luteinizing hormone (LH), and follicle-stimulating hormone (FSH) under normal and irradiated states. (E) Decreased sperm DNA integrity and (F) sperm motility after radiation. (G) Levels of the sperm morphology indexes included arc, head width, head area, head circumference, linearity, angle, degree of head fold, midpiece width, and midpiece insertion angle under normal and irradiated states. (H) Decreased lactate dehydrogenase (LDH), succinic dehydrogenase (SDH), and adenosine triphosphate (ATP) synthase levels after radiation. (I) Levels of superoxide dismutase (SOD) activity and malondialdehyde (MDA) under normal and irradiated states. (J) Hematoxylin-eosin (HE) staining of testicular tissue showed morphological changes, revealing cavitation of spermatogonia, disturbed cell arrangement, and interstitial edema after radiation. Scale bars = 50 μm. (K-N) Transmission electron microscopy shows ultrastructural changes in testicular tissue, such as chromatin condensation and border migration in spermatocytes after radiation, uneven chromatin distribution in the spermatids, as well as edema and vacuolation of mitochondria in the spermatogonia, spermatocytes, and the round spermatids. Scale bars = 2 μm or 5 μm. Experiments were repeated at least three times. Data are mean values ± SD. *$P < 0.05$, * *$P < 0.01$, * **$P < 0.001$ (two-tailed t test).

analyze the enrichment scores of different pathways. The results showed that activation of the innate immune response, response to decreased oxygen levels, response to progesterone, sperm capacitation, urate metabolic processes, parathyroid hormone synthesis, secretion, and action pathways were significantly enriched in irradiated rats (Fig. 2D-E; Table S2).

3.3. Effects of long-term microwave radiation on the metabolic phenotypes of testicular tissues

Previous studies have shown that energy metabolism play considerable roles in microwave-induced damage in male rats (Men et al., 2023). We conducted a metabolomic analysis on rat testicular tissues after microwave irradiation. The radiation-treated samples and control groups exhibited significant differences in the PCA score plot. The pooled quality control samples clustered in positive and negative ion modes, demonstrating distinct intra-group clustering and inter-group separation, indicating high stability and reproducibility of the analysis (Figs. 3A and 4A).

A total of 533 metabolites in positive ion mode and 549 metabolites in negative ion mode were identified. In comparing the irradiated and control groups, 42 metabolites in the positive and 32 in the negative ion modes were significantly altered. Specifically, there were 37 upregulated and five downregulated metabolites in the positive ion mode, while 18 and 14 were upregulated and downregulated in the negative ion mode (Figs. 3B-D and 4B-D). These results seemingly demonstrated that radiation impacts the regulation of oxidative stress-related cellular factors, such as the glutathione precursor Cys-Gly and flavin mononucleotide, which serve as components of the electron transport chain, helping to maintain the cellular redox state and thereby reduce the potential damage of oxidative stress to cells. Systematic pathway annotation for all identified metabolites showed that DEMs were enriched in autophagy, glycerophospholipid metabolism, glutathione metabolism, vitamin digestion and absorption, ferroptosis, biosynthesis of unsaturated fatty acids, oxidative phosphorylation, nicotinate and nicotinamide metabolism (Figs. 3E and 4E).

3.4. Cell type annotation of scRNA-seq clusters in testicular tissue

To better understand the effects of microwave radiation from single cell resolution, scRNA-seq and scATAC-seq profiles of the testicular tissues from irradiated and control rats were generated to acquire specific transcriptional profiles for each cell subpopulation. Following rigorous quality control (Fig. 5A and Fig. S1A-D), 23,384 cells were clustered into 10 cell subgroups (Fig. 5B-C). According to the known marker genes (Fig. 5C-D; Table S3), these clusters were defined as spermatocytes (Ddx4 or Glipr1l1), round spermatids (Ddx4/Glipr1l1 and largely Pde4a), spermatids (Tbc1d20), elongating spermatids (Tbc1d20 and Prss58), testicular peritubular cells ($Vim^{+}/Id2^{-}/Vwf^{-}$), spermatogonia (Dazl), smooth muscle cells (Acta2 and Id2), macrophages (Cd74), endothelial cells (Vwf), or Sertoli cells (Sox9). Germ cells were the main component of testicular tissue (83.8 %). Radiation caused changes in the proportion of cell types (Fig. 5C and Fig. S1B). Specifically, we observed a decrease in spermatocytes (23.0 % in the irradiated group vs. 25.4 % in the control group), elongated spermatids (13.8 % vs. 15.4 %), and spermatids (18.8 % vs. 20.9 %); an increase in round spermatids (23.6 % vs. 18.3 %); and no apparent change in spermatogonia (4.4 % vs. 4.0 %) after radiation. Furthermore, we observed a decrease in testicular peritubular cells (6.3 % vs. 7.4 %) and endothelial cells (2.3 % vs. 2.6 %) and a slight increase in smooth muscle cells (3.9 % vs. 3.0 %) and macrophages (3.4 % vs. 2.9 %) in the irradiated group. The proportion of Sertoli cells was remarkably higher after radiation; however, the total number of cells was low (0.26 %). In summary, we observed changes in cell composition associated with radiation. These changes appeared most significantly in germ cells, especially stuck in round spermatids, suggesting potential reproductive effects of radiation exposure during spermatogenesis.

3.5. Cell-type annotation and genetic changes of scRNA-seq germ subpopulations

We classified the five phases of germ cell development according to the following marker genes: spermatocytes (Limch1 and Pde4a), spermatids (Tbc1d20), round spermatids (Spaca1), elongated spermatids (Ctdspl4), and spermatogonia (Dazl and Stra8) (Fig. 6A-B and Fig. S2A, S2B). We then identified DEGs from each germ cluster in the control and irradiated groups. By comparing the amount of DEGs, we found that radiation had the greatest effect on the transcriptome profiles of spermatogonia and spermatocytes, followed by that of spermatocytes (Fig. 6C). Most DEGs were cell-type-specific (e.g., spermatogonia: 609). However, some upregulated genes were simultaneously present in two or more somatic cell types (65 genes were present in four or five cell types, and 322 genes were present in two or three cell types), suggesting a degree of commonality among germ cells. To further explore the impact of radiation on biological processes, we calculated the degree of enrichment of GO and KEGG pathways for the five germ subpopulations (Fig. 6D and Fig. S2C). Volcano plots were used to analyze the expression of DEGs in spermatids (upregulated: 109; downregulated: 129), round spermatids (upregulated: 209; downregulated: 200), and spermatogonia (upregulated: 82; downregulated: 670) in the irradiated group (Fig. 6E and Fig. S2D). Cmtm2a is associated with the negative regulation of testosterone synthesis and is downregulated in round spermatids after microwave radiation (Qamar et al., 2009). In spermatogonia, Stt3b, which is involved in cellular protein metabolism, was downregulated in irradiated rats (Sato et al., 2012), whereas Btg1, which is related to the oxidative stress pathway and affects spermatogenesis, was upregulated (Raburn et al., 1995). In addition, Cftr, identified as a DEG by bulk RNA-seq analysis, was upregulated in spermatocytes, round spermatids, and elongating spermatids after microwave radiation (Fig. S2D).

3.6. Validation of genetic changes in germ cells receiving microwave radiation

In spermatogonia cells, we observed significantly downregulated expression of Rpl4, which belongs to the L4E family of ribosomal proteins located in the cytoplasm and encodes ribosomal proteins (Bagni et al., 1993). For validation, we used Dazl (Fig. 7A) as a marker gene for

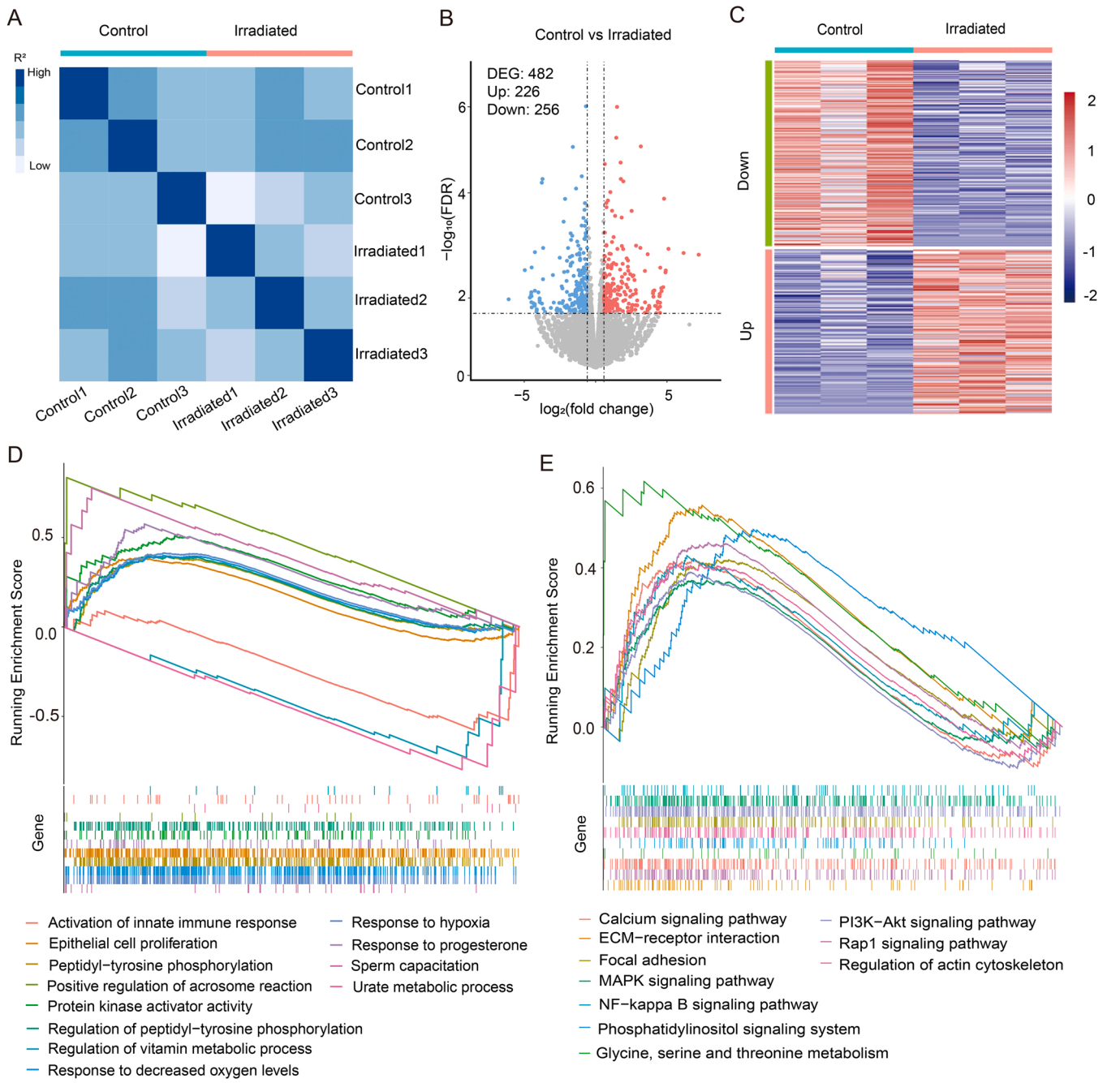

Fig. 2. Identification of differentially expressed genes between long-term microwave radiation and control groups based on bulk RNA-seq data. (A) Heatmap of the pairwise Pearson's correlation between each sample. (B) Volcano plot showing immune-related DEGs between groups. Red and blue dots represent upregulated and downregulated immune genes in the irradiated group. (C) Heatmap of DEGs for testicular tissues. Different colors indicate the Degree of expression, with expression increasing between blue and red: blue indicates low expression, and red indicates high expression. (D and E) Gene Set Enrichment Analysis (GSEA) for Gene Ontology (GO) and Kyoto Encyclopedia of Genes and Genomes (KEGG) enrichment between control and irradiated groups. Up: curves of enrichment score changes for predefined gene sets in different functional units across the cumulative process. Each line indicates one functional unit marked with a specific color. Down: location of the gene members of predefined gene sets in the functional units, with arrows showing the direction of enrichment in the control and irradiated groups. Functional units associated with immune function ($P < 0.05$) are presented.

spermatogonia inside seminiferous tubules, which was labeled Rpl4 with FISH probes (Fig. 7B). We found that the expression of Rpl4 decreased after radiation (Fig. 7C). Dazl was downregulated in spermatogonia after radiation. A previous study showed that Dazl plays a crucial role during embryonic germ cell development and differentiation and is a hallmark of vertebrate germ cells (Li et al., 2019). We then re-analyzed the spermatogonia clusters from Fig. 7D. As previously observed, spermatogonia were divided into four subtypes, from SPG1 to SPG4 (Green et al., 2018). Marker gene analysis suggested that SPG1 represents undifferentiated spermatogonia, as expressed by spermatogonial stem cell genes such as Id4, and lacks the expression of differentiation markers (Fig. 7E). Cells in the SPG2–4 subtypes expressed various combinations of differentiation marker genes. Like the cells in SPG4, these cells expressed high levels of Kit, Stra8, and meiotic genes (such as Sycp3 or Prdm9). The proportions of each cell type are shown in Fig. 7F. Similarly, we used Spaca1 (Fig. 7G) as a marker gene for round spermatids then separately labeled Camk4, Spaca7, and Atp6v1e2 with FISH probes (Fig. 7H), and the results showed increased expression after

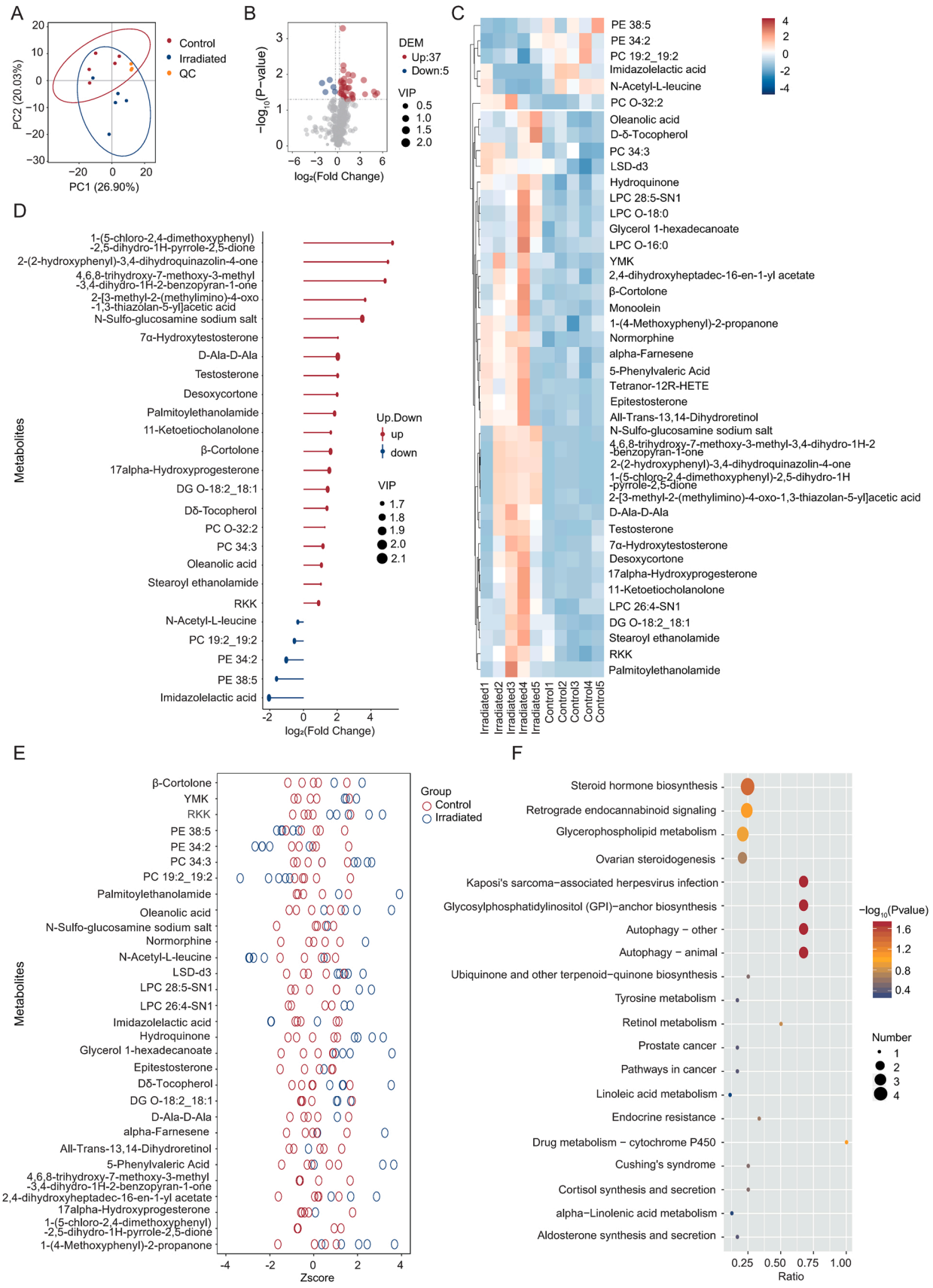

Fig. 3. Effects of radiation on the metabolic phenotypes of testicular tissues in positive mode. (A) PCA score plot for all the control (red), irradiated (blue), and QC (orange) samples. (B) Volcano plot to identify the DEMs in testicular tissues with and without radiation treatment. (C) Heatmap plot of the DEMs in the irradiated and control groups. (D) Stem plot of the DEMs. (E) Z score plot of the DEMs in the irradiated and control groups. (F)The effects of radiation on the KEGG pathways.

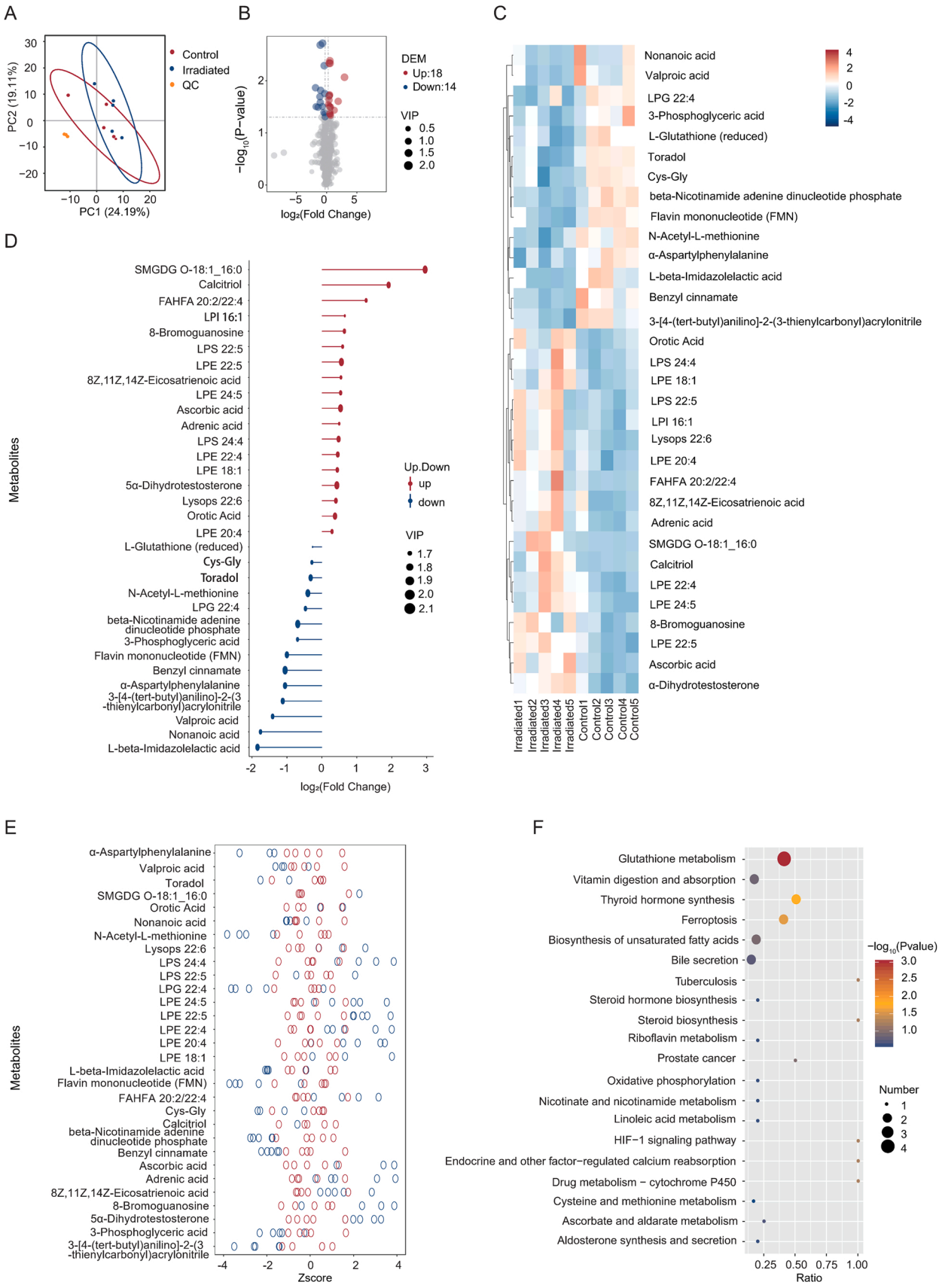

Fig. 4. Effects of radiation on the metabolic phenotypes of testicular tissues in negative mode. (A) PCA score plot for all the control (red), irradiated (blue), and QC (orange) samples. (B) Volcano plot to identify the DEMs in testicular tissues with and without radiation treatment. (C) Heatmap plot of the DEMs in the irradiated and control groups. (D) Stem plot of the DEMs. (E) Z score plot of the DEMs in the irradiated and control groups. (F)The effects of radiation on the KEGG pathways.

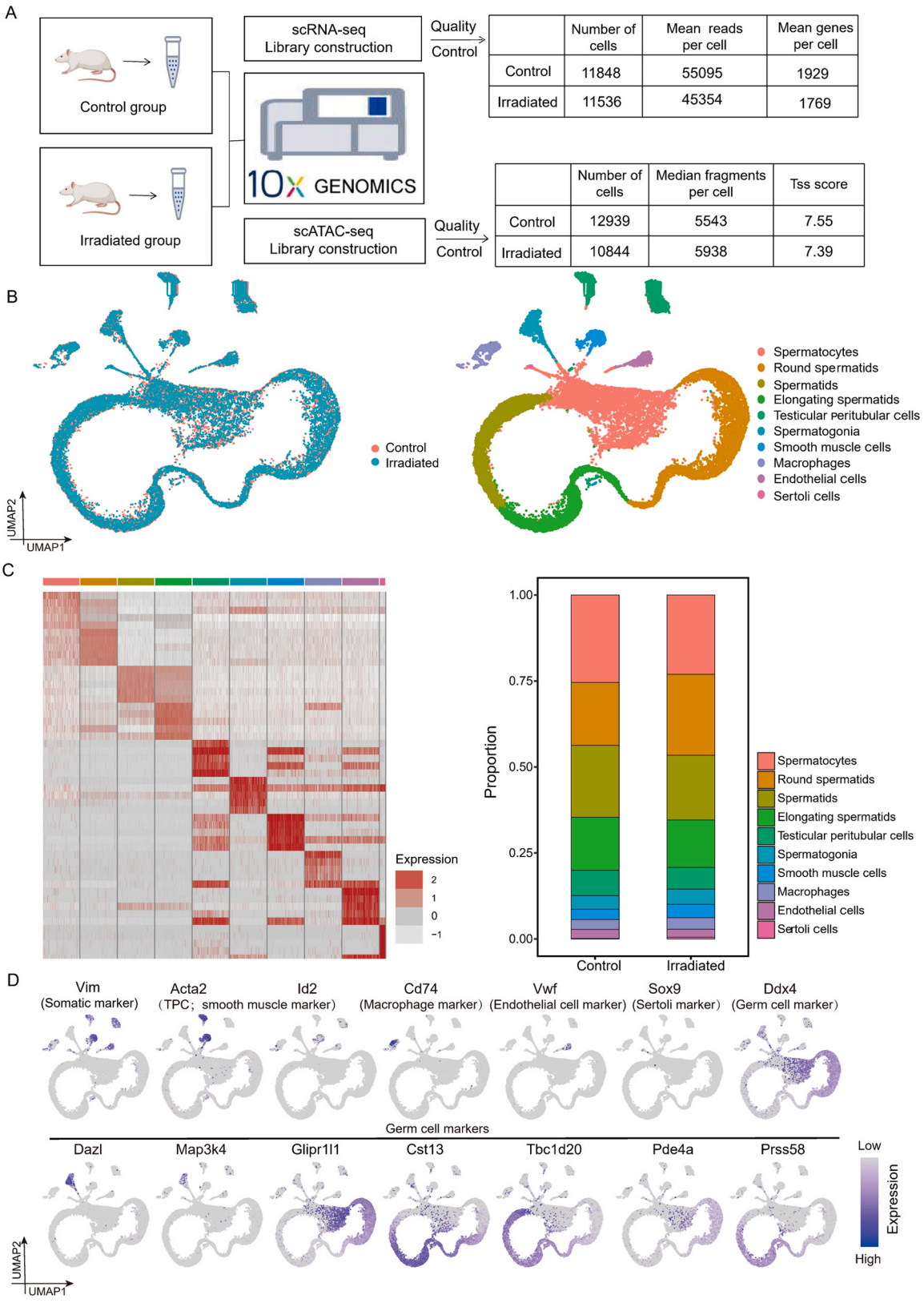

	Number of cells	Mean reads per cell	Mean genes per cell
Control	11848	55095	1929
Irradiated	11536	45354	1769

	Number of cells	Median fragments per cell	Tss score
Control	12939	5543	7.55
Irradiated	10844	5938	7.39

Fig. 5. Major cell types and cellular attributes inferred using scRNA-seq analyses of the rat testis after radiation. (A) Workflow of study design and quality control. (B) UMAP plot of testicular cell clusters defined by scRNA-seq analysis from control and irradiated rats. Each dot represents a single testicular cell and is colored based on its donor of origin. (C) Left: DEGs heatmap of cell-type-specific transcripts by cluster from (B). Scaled gene expression levels are colored according to the Z score. Right: percentage of cells within each cluster from (B) using bar plot. Cluster colors match those in (B). (D) Representative enriched genes identifying major testicular cell types cast on the UMAP plot. Purple corresponds to a high expression level; gray corresponds to a low expression level.

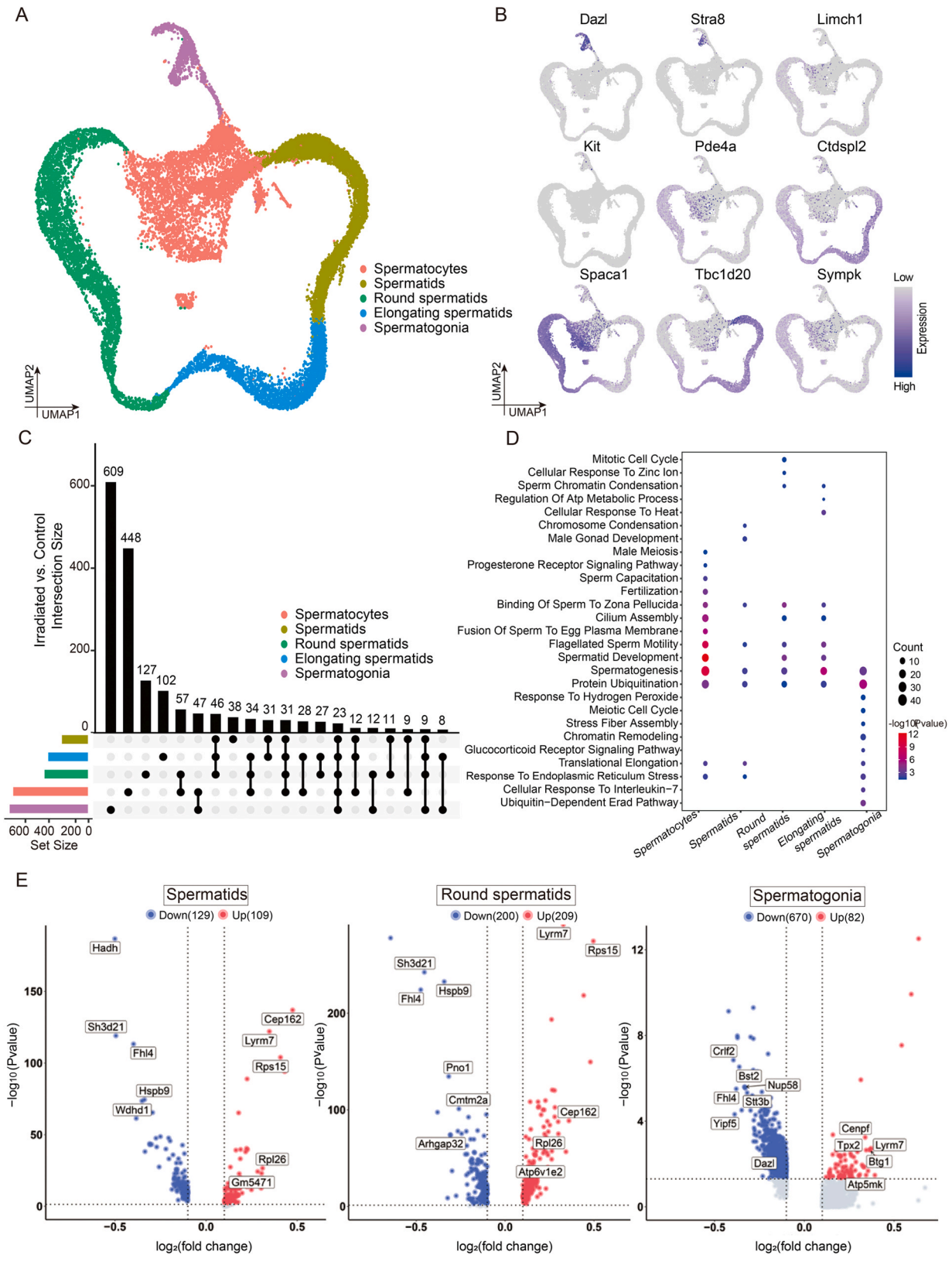

Fig. 6. Identification of germ cell types and DEGs between irradiated and control groups with scRNA-seq. (A) Annotated germ cells were captured using UMAP, as shown in Fig. 3B. (B) Expression patterns of selected markers are cast on the UMAP plot in (A). Purple corresponds to a high expression level; gray corresponds to a low expression level. (C) Integrated comparative analysis of DEGs in germ clusters between control and irradiated groups using UpSet plot. Horizontal bars on the left show the number of DEGs for each cluster labeled with different colors. A single dot indicates the DEG set specific to a cell cluster. Lines between clusters highlight shared DEGs. Vertical bars on the top represent the number of DEGs. (D) GO analysis of DEGs in germ clusters using DAVID. Dot size indexes the number of DEGs in the corresponding pathway. Color bars show *P*-values. (E) DEGs in spermatids, round spermatids, and spermatogonia using a volcano plot.

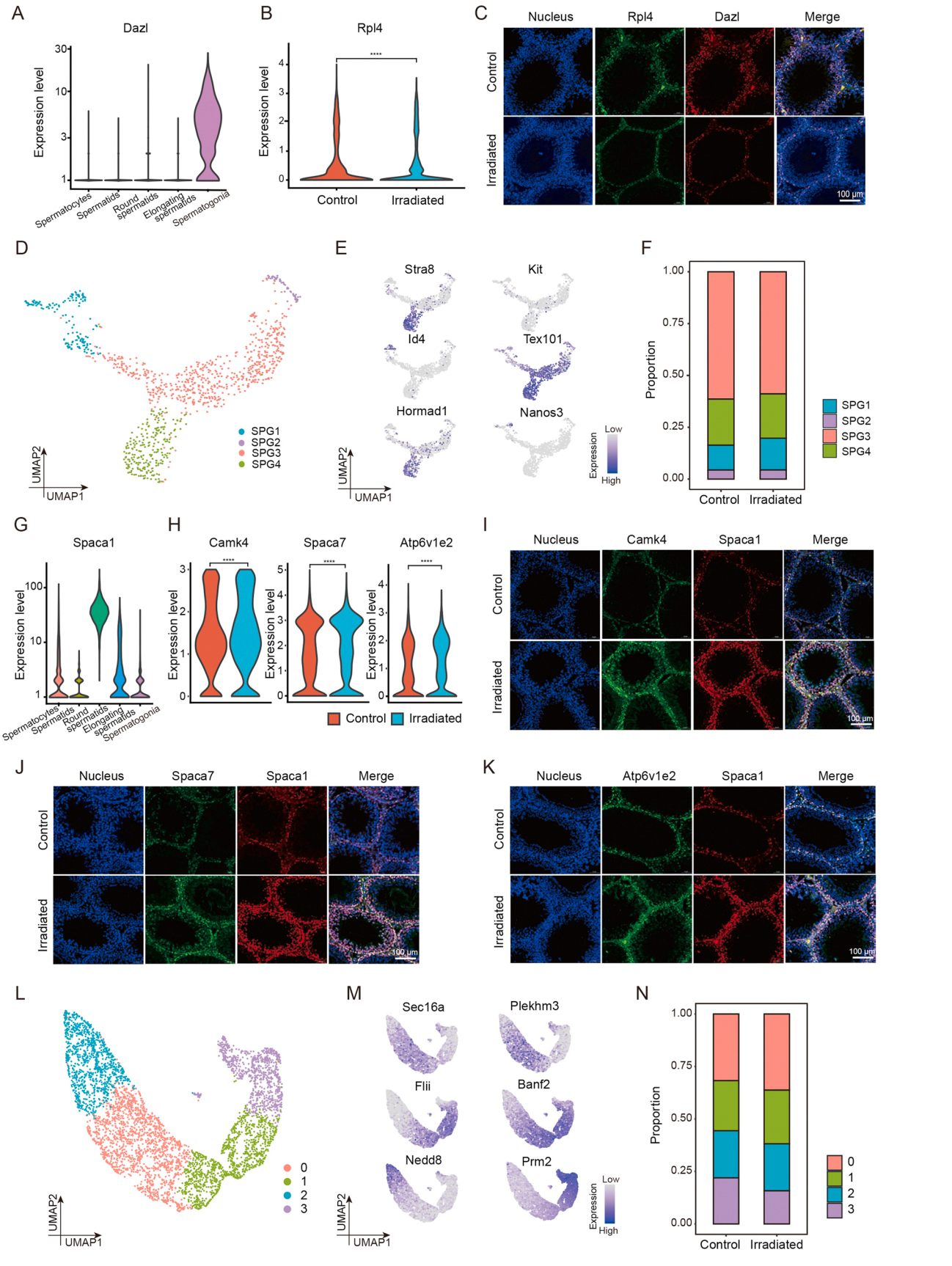

(caption on next page)

Fig. 7. Subtype analysis and experimental verification in partial germ clusters after radiation. (A) Violin plots showing Dazl as a marker gene of spermatogonia cells. (B) Violin plots showing Rpl4 as the DEG of spermatogonia between the control and irradiated groups. (C) Decreased expression of Rpl4 (green) and Dazl (red) in the irradiated group using the FISH assay. Cell nuclei were stained with DAPI (blue). Scale bars = 100 μm. (D) UMAP plot of spermatogonia cell subtypes derived from scRNA-seq analysis. Each dot represents a single spermatogonia cell. (E) Representative enriched genes identifying spermatogonia subtypes cast on the UMAP plot. Purple (gray) corresponds to a high (low) expression level. (F) Bar plot showing the percentage of each subtype of spermatogonia. (G) Violin plots showing Spaca1 as a marker gene of round spermatids. (H) Violin plots showing Camk4, Spcaca7, and Atp6v1e2 as DEGs of round spermatids between the control and irradiated groups. (I—K) Elevated expression of Camk4 (I), Spcaca7 (J), and Atp6v1e2 (green), Spaca1 (red) (K) in the irradiated group using the FISH assay. Nuclei were counterstained with DAPI (blue). Scale bars = 100 μm. (L) UMAP plot of round spermatids subtypes derived from scRNA-seq analysis. Each dot represents a single cell of round spermatids. (E) Representative enriched genes identifying subtypes of round spermatids cast on the UMAP plot. Purple (gray) corresponds to a high (low) expression level. (F) Bar plot showing the proportions of each cell subtype of round spermatids.

radiation (Fig. 7I-K). Spaca1 encodes sperm acrosome-associated protein 1, which exists in the acrosome at all stages of sperm development, such as the Golgi and apical cap stages of round spermatids (Jones et al., 2008), and was upregulated in round spermatids after radiation. Atp6v1e2 encodes the second isoform of the E subunit of the V-ATPase complex (Van Damme et al., 2017), which has a binding site in the promoter region of transcription factor Cebpb identified as a DEG of our Bulk RNA-seq. We further performed subtype analysis and observed that cells in the round spermatids were partitioned into four groups (Fig. 7L). Cell-type-specific marker genes and their proportions are represented in Figs. 7M and N. After examining the known conserved marker genes in each cluster, we identified four cell subtypes of spermatocytes (Figs. S3A-C) following the expression of marker genes (Hspa5 and Pnma8b) (Fig. S3D). In spermatids, we observed three cell subtypes (Figs. S3E-G) following the expression of marker genes (Aif1 and Gm5471) (Fig. S3H). In addition, the three subgroups were clearly distinguished in elongating spermatids using the marker genes Tnp1 and Fancd2os (Figs. S3I-L). The proportion of subtypes of each cell type showed an intuitive change after irradiation (Figs. S3B, F, and J).

3.7. Features of cell-cell communication patterns after microwave radiation

CellChat was used to explore cell-cell communication. We found that the interaction quantity and strength were integrally attenuated among cell clusters from the control group to the irradiated group (Fig. 8A-B, and Figs. S4A-B). We observed obvious changes in cellular communication in different signaling pathways. Radiation-inhibited laminin signaling between somatic cell subsets and somatic-to-germ cell subsets was remarkably weakened after radiation (Fig. 8C). However, radiation stimulated collagen signaling between Sertoli cells and somatic subpopulations (Fig. 8D). As mentioned previously, the proportion of round spermatids increased after radiation. We further used receptor-ligand analysis to confirm the changes in these signaling pathways in cell communication from round spermatids to other cells (Fig. 8E). We observed that Col6a1-(Itga9 +Itgb1) signaling seemed to be selectively dysregulated in peritubular myoid cells, whereas Lamb3-Dag1 signaling seemed to be dysregulated in spermatogonia, suggesting that radiation significantly altered laminin and collagen secretion patterns. We also elucidated the total communication patterns in irradiated and control groups based on the four key patterns of outgoing (treating cells as senders) and incoming (treating cells as receivers) signaling (Fig. 8F, and Figs. S4C-D). As expected, radiation altered cellular signal patterns. For instance, the outgoing signaling of Sertoli and endothelial cells in the control group was characterized by patterns 1 and 2, representing pathways such as Jam, Cldn, Visfatin, and Sema7 (pattern 1), and Cxcl, Notch, and Cd39 (pattern 2) signaling, respectively; however, these patterns were exchanged with each other after radiation. The incoming signaling of testicular peritubular cells in the radiation group was remarkably weakened in pattern 3 (Fig. 8F).

3.8. Chromatin accessibility of testicular tissues exposed to radiation

We explored the differences in chromatin accessibility of scATAC-seq between irradiated and control groups (Fig. 9A). Integrative analysis of scRNA-seq and scATAC-seq data implied that cells in round spermatids in the scATAC-seq results were primarily transferred to spermatocytes. Moreover, we observed cell specificity by detecting the marker genes of ATAC peaks (Fig. 9B). To assess changes in gene regulation programs after radiation, we further calculated and compared the differential ATAC peaks and DNA motif enrichment across each cell population from control to irradiated cells. Significantly underrepresented or overrepresented motifs between radiation exposure and control groups were revealed using DNA motif scanning of the differential regions (Fig. 9C). Compared with the control, the Rpl4 gene motifs for KLF9, FOXK2, and IRF9 were significantly repressed in spermatogonia cells (Fig. 9C). Several enriched motifs in the irradiated group were common to most somatic and germ cells, reflecting global transcription factor circuitry perturbations (e.g., FOXD1, NKX6–1, HLTF, KLF6, and KLF5) (Fig. 9C). These differential regulatory regions perturbing different cell types were enriched in genes such as Ccdc54, Rpl4, Lrrtm4, and Sqle (Fig. 9D). Generally, our data uncovered 666 irradiation-specific regulatory regions that may affect the response to radiation.

4. Discussion

Electromagnetic pollution is the fourth major source of pollution in modern society after water, air, and noise pollution, and its health hazards have been studied for several years. As early as 2012, the Independent Advisory Group on Non-Ionizing Radiation of the Health Protection Agency in the United Kingdom pointed out that many studies have investigated the effects of radiofrequency fields on testicular function, mainly in rats, and most reports have found significant effects.

However, to date, the impacts of microwave exposure on male reproduction have not been fully elucidated (Tumkaya et al., 2016; Yu et al., 2020). Considering the high possibility of long-term exposure to microwave radiation for personnel working in communication base stations and radar systems (Balmori, 2022; Peleg et al., 2023) and residents living nearby. This study explored these effects in adult rats by simulating the special situation of long-term high-power pulsed microwave exposure. This model minimized the effects of heat and stress on reproduction. A significant finding of our study is the effect of long-term exposure to high-power pulsed microwave radiation on rat testes and reproductive capacity, which has not been previously reported. The effects on fertility were assessed by examining hormone levels and semen quality, including DNA damage, sperm motility, sperm morphology, and structure. Our results indicated that continuous exposure to microwave radiation with an average power density of 30 mW/cm^2, a frequency of 2.856 GHz, and an average SAR of 19.8 W/kg for 15 min/day, five days a week for six weeks resulted in interference with androgens, decreased sperm motility, abnormal sperm morphology, DNA damage and impaired testicular tissue structure and ultrastructure in rats, which suggests long-term microwave radiation had negatively impacts on the reproductive health of male rats and can significantly impair the fertility.

We further performed bulk RNA-seq to characterize the DEGs and pathway enrichment in testicular tissues exposed to long-term microwave radiation. Enrichment of the calcium and PI3K-Akt signaling pathways was related to spermatogenesis and oxidative stress (Yuan et al., 2022; Zhang et al., 2023), which was reflected in the following

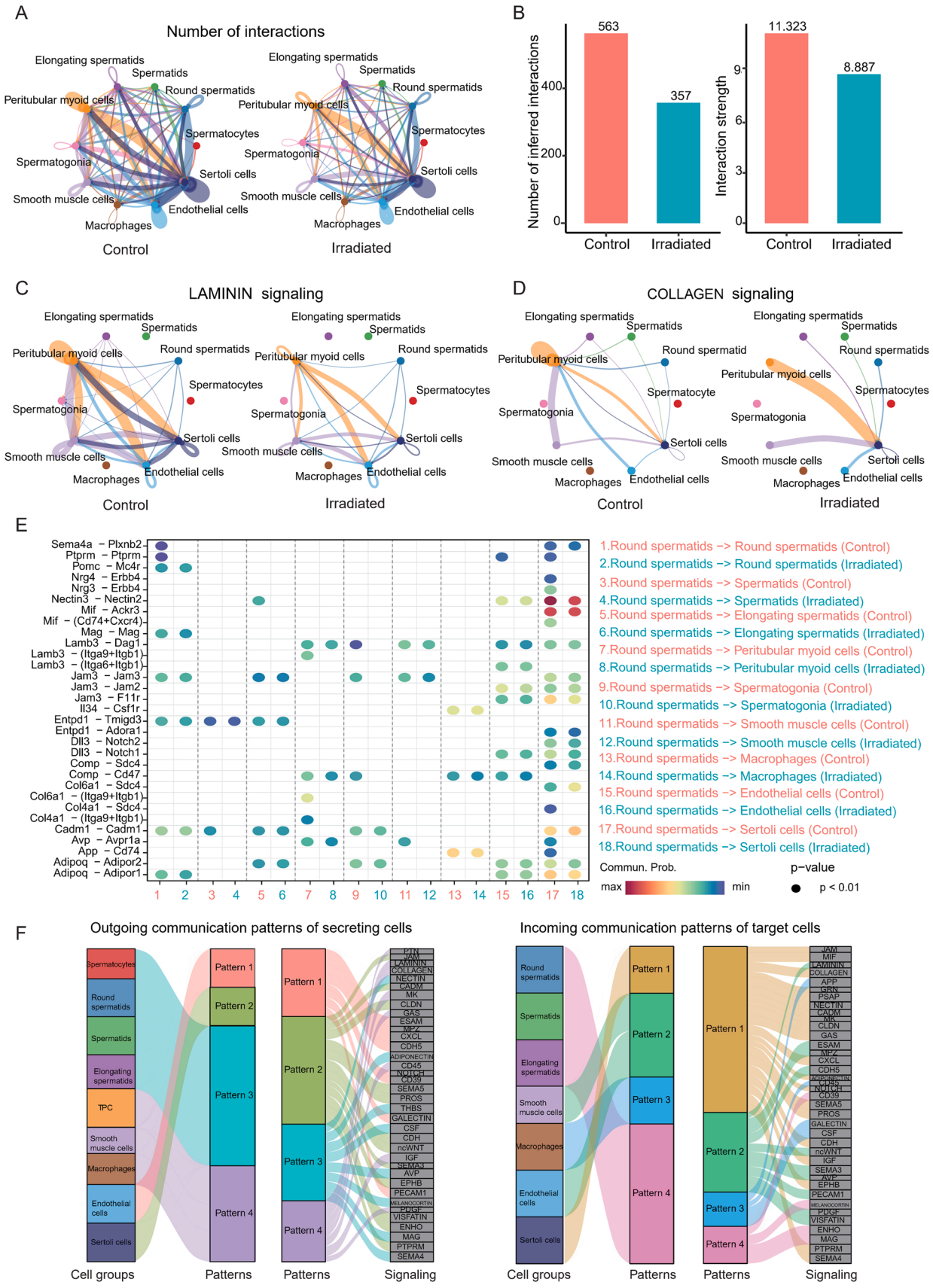

(caption on next page)

Fig. 8. CellChat analysis of the communications between rat testis cells identified using scRNA-seq. (A) Circle plot showing the inferred cell-cell communication networks between the control and irradiated group. Edge width represents the communication probability. Edge colors are consistent with the signaling source, and edge width indicates the probability of communication. (B) Bar plots showing the inferred interactions and strengths between control and irradiated groups. The inferred laminin signaling network (C) and collagen signaling network (D) in control and irradiated groups. Arrows show the signal transmission direction from the source to the target. (E) Comparison of the significant ligand-receptor pairs of laminin, collagen, and other signaling pathways from round spermatids to other cell types between control and irradiated groups. Color bar reflects communication probabilities. Dot sizes represent *P*-values. (F) The inferred outgoing communication patterns of target cells (left) and incoming signaling patterns of secreting cells (right) in the irradiated group using alluvial plots. Thickness of the flow indicates the contribution of the cell group or signaling pathway to each latent pattern.

phenotype: decreased SOD activity, increased MDA level, and decreased sperm motility in the radiation group. Glycine, serine, and threonine metabolism, phosphatidylinositol signaling systems, and endocrine resistance regulated metabolism were consistent with the reduced levels of LDH, SDH, and ATP synthase in irradiated rats, indicating the impacts of energy metabolism after radiation (Du et al., 2022; Schiavi-Ehrenhaus et al., 2022). The similarity was found in metabolomics analysis, and differentially expressed metabolites were enriched in autophagy, oxidative phosphorylation, nicotinate, and nicotinamide metabolism. Induced oxidative stress and disturbed energy metabolism may be potential mechanisms in radiation-induced reproductive damage.

Given the above observations of phenotypes, bulk RNA-seq, and metabolomics analysis after long-term radiation, we conducted scRNA-seq and scATAC-seq analyses to characterize cell-specific changes in the transcriptional profile and biological processes after long-term microwave radiation. Formerly, well-defined markers were used to identify the germ and somatic cell types in 10 clusters generated by UMAP analysis (Green et al., 2018; Tan et al., 2020). Microwave radiation significantly increased the percentage of round spermatid cells, suggesting that radiation impacted sperm development and stagnated the differentiation of round spermatids.

According to our findings, we postulate several reasons for the stagnation of round spermatids. In the first place, pathway enrichment analyses showed that the Rap1 signaling pathway, the synthesis, secretion, and action of parathyroid hormone, and the PI3K-Akt signaling pathway were abnormal after microwave exposure, resulting in a decrease in serum testosterone levels, which may affect further differentiation of round spermatid cells. When intra-testicular testosterone was suppressed, the transformation of round spermatids between stages VII and VIII of the spermatogenic cycle was significantly inhibited, and elongated spermatids were not detected (L et al., 1994, 1996). Furthermore, the expression of Atp6v1e2, the isoform of the V-ATPase subunit E, was specifically increased in the round spermatids. Pathway analyses showed abnormal regulation of ATP metabolism after microwave exposure. Atp6v1e2 created an electrochemical proton gradient across eukaryotic cell membranes to energize fundamental cellular processes and primarily utilizes the energy derived from ATP hydrolysis to pump protons (H^+) across the cell membrane, thereby influencing cellular metabolism and membrane transport processes. The transcription factor Cebpb was significantly upregulated following irradiation revealed by bulk RNA-seq, which has binding motifs within the promoter region of the Atp6v1e2 gene, which suggests that Cebpb may serve as a transcriptional regulator to facilitate the upregulation of Atp6v1e2 expression following irradiation, thus regulating energy metabolism and affecting male reproduction. Last but not least, the sperm acrosome-associated proteins Spaca7 and Spaca1 showed increased expression (L et al., 1994; Zhang et al., 2020). Spaca7 encodes sperm acrosome-associated protein 7, which is exclusively expressed in the testes (Korfanty et al., 2012). Spaca7 is also a male germ cell-specific protein in the sperm acrosome and plays a role in mouse fertilization (Nguyen et al., 2014). The expression of Spaca7 has significant cell specificity and is highly expressed in round sperm, localized at perinuclear points near the Golgi apparatus and acrosome of elongating spermatids and spermatozoa (Nguyen et al., 2014; Aisha and Yenugu, 2023). Our study also validated the cell specificity of Spaca7 in round spermatids at the single-cell level and found that its expression was significantly upregulated after long-term radiation.

Moreover, integrative scRNA-seq and scATAC-seq analysis of rat testicular cells implied a relationship between gene expression and chromatin accessibility, and multiple subpopulations exhibited differences in overall chromatin accessibility and lineage-specific transcription factor activity, particularly the potential role for Rpl4 after radiation. Rpl4 belongs to the L4E family of ribosomal proteins in the cytoplasm and encodes ribosomal proteins (Bagni et al., 1993). Ribosomes are sites of RNA translation and protein synthesis. Previous studies have indicated that the ribosomal protein L4 is critical in coordinating ribosome biogenesis with cell growth and proliferation (He et al., 2016). Many studies have revealed that the Rpl4 protein is inextricably linked to the expression, ubiquitination, and regulation of various proto-oncogenes, signaling pathways, protein translation, and apoptosis (Liu et al., 2024). In our study, scRNA-seq and scATAC-seq analyses and FISH experiments revealed that Rpl4 was associated with male reproductive damage caused by microwave radiation (such as abnormal spermatogonia number), suggesting that Rpl4 may be a marker gene for male reproductive damage caused by microwave radiation.

5. Conclusions

Our study aimed to reveal the impact of long-term microwave radiation on testicular tissues and characterize the associated transcriptional and metabolic profile changes. Our results highlight that: long-term microwave radiation may impair the testes and male reproductive potential of rats predominantly through male hormone disruption, decreased sperm motility, abnormal sperm morphology, DNA damage, damage to the testicular tissue structure and ultrastructure, enhanced oxidative stress, and disrupted energy metabolism; microwave radiation influenced sperm development and stagnated round spermatids; and radiation caused key transitions involving genes, cell-cell communication and metabolism. Our study provides an effective framework for future investigations of the impact of long-term microwave-related radiation on male fertility, as well as new insights and targets for the protection and treatment of microwave exposure injury in human populations with occupational exposure.

CRediT authorship contribution statement

Li Yanyang: Investigation. **Wang Heran:** Writing – review & editing. **Pang Yueyue:** Writing – original draft. **Men Junqi:** Writing – original draft, Investigation. **Liu Jing:** Investigation. **Hui Wang:** Investigation. **Zhao Li:** Investigation. **Fan Jiao:** Writing – review & editing, Supervision, Project administration, Conceptualization. **Zeng Jing:** Writing – original draft. **Shi Jingqi:** Writing – original draft. **Li Chunlin:** Writing – review & editing, Supervision, Conceptualization. **Peng Ruiyun:** Writing – review & editing, Supervision, Conceptualization. **Yao Binwei:** Writing – original draft.

Declaration of Competing Interest

The authors declare that they have no known competing financial interests or personal relationships that could have appeared to influence the work reported in this paper.

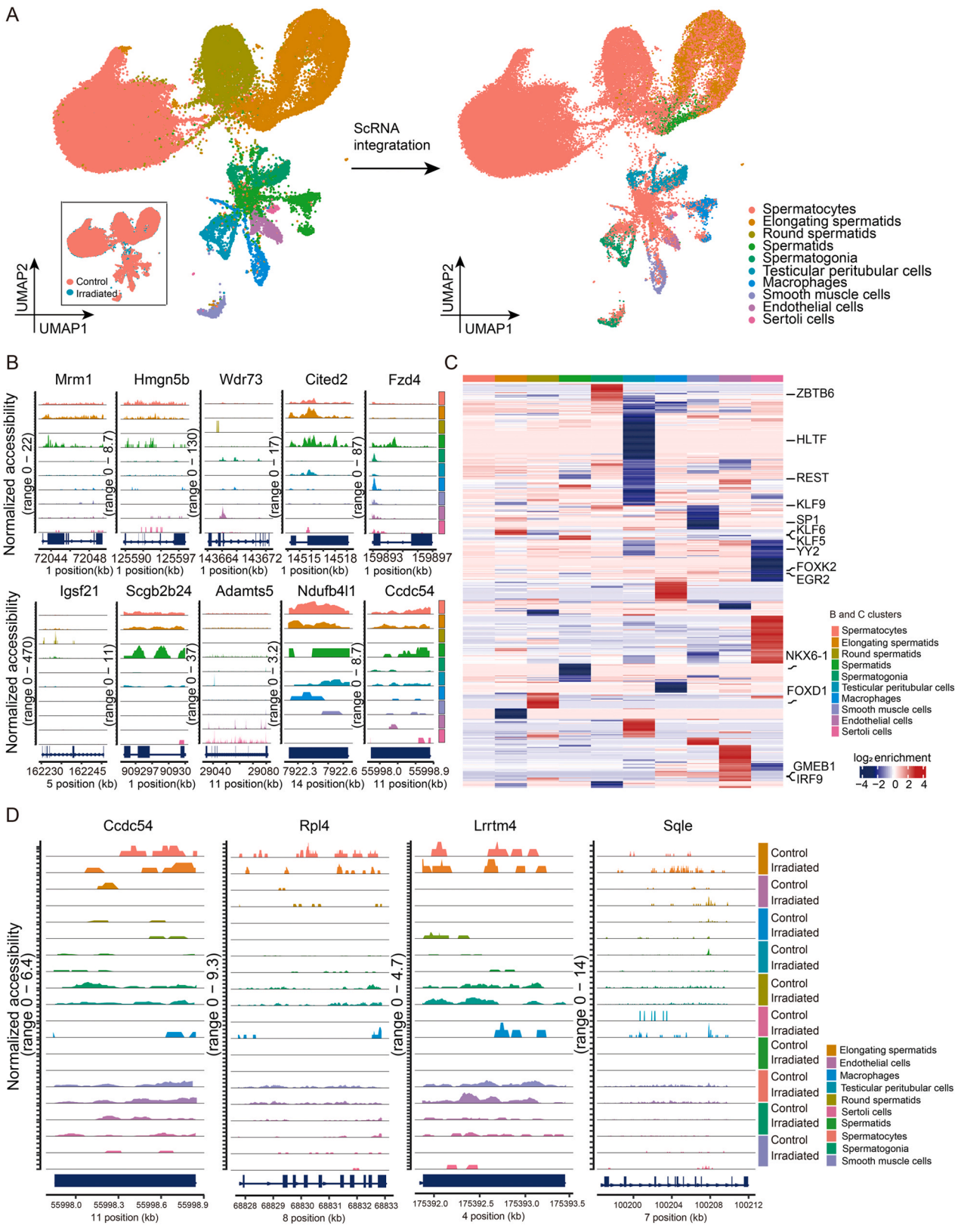

Fig. 9. Cell type-specific differences in chromatin accessibility between control and irradiated groups. (A) UMAP visualization of the scATAC-seq dataset (71,509 single cells), annotating clusters based on previous scRNA-seq markers with Signac. (B) Normalized chromatin accessibility profiles for each cell type at marker genes. Gene model and chromosome position below highlight the promoter region in blue. Cluster colors match those in (A). (C) Heatmap representation of DNA motifs with differential enrichments between irradiated and control groups across all scATAC-seq clusters. Associated motifs are highlighted on the right. (D) Coverage plots of selected loci split by cell type and condition.

Appendix A. Supporting information

Supplementary data associated with this article can be found in the online version at doi:10.1016/j.ecoenv.2025.118040.

Data availability

Data will be made available on request.

References

Aisha, J., Yenugu, S., 2023. Characterization of SPINK2, SPACA7 and PDCL2: Effect of immunization on fecundity, sperm function and testicular transcriptome. Reprod. Biol. 23, 100711. https://doi.org/10.1016/j.repbio.2022.100711.

Bagni, C., Mariottini, P., Annesi, F., Amaldi, F., 1993. Human ribosomal protein L4: cloning and sequencing of the cDNA and primary structure of the protein. Biochim Biophys. Acta 1216, 475–478. https://doi.org/10.1016/0167-4781(93)90017-8.

Balmori, A., 2022. Evidence for a health risk by RF on humans living around mobile phone base stations: from radiofrequency sickness to cancer. Environ. Res. 214, 113851. https://doi.org/10.1016/j.envres.2022.113851.

Belpomme, D., Hardell, L., Belyaev, I., Burgio, E., Carpenter, D.O., 2018. Thermal and non-thermal health effects of low intensity non-ionizing radiation: an international perspective. Environ. Pollut. 242, 643–658. https://doi.org/10.1016/j.envpol.2018.07.019.

Bernabò, N., Ciccarelli, R., Greco, L., Ordinelli, A., Mattioli, M., Barboni, B., 2017. Scientometric study of the effects of exposure to non-ionizing electromagnetic fields on fertility: a contribution to understanding the reasons of partial failure. PLoS One 12, e0187890. https://doi.org/10.1371/journal.pone.0187890.

Du, Z., Li, W., Liu, C., Wang, C., Wang, D., Zhu, S., Kang, X., Jiang, R., Deng, L., Li, D., Sun, G., 2022. Transcriptome analysis of the testes of male chickens with high and low sperm motility. Poult. Sci. 101, 102183. https://doi.org/10.1016/j.psj.2022.102183.

Green, C.D., Ma, Q., Manske, G.L., Shami, A.N., Zheng, X., Marini, S., Moritz, L., Sultan, C., Gurczynski, S.J., Moore, B.B., Tallquist, M.D., Li, J.Z., Hammoud, S.S., 2018. A comprehensive roadmap of murine spermatogenesis defined by single-cell RNA-Seq. e10 Dev. Cell 46, 651–667. https://doi.org/10.1016/j.devcel.2018.07.025.

Guo, J., Grow, E.J., Mlcochova, H., Maher, G.J., Lindskog, C., Nie, X., Guo, Y., Takei, Y., Yun, J., Cai, L., Kim, R., Carrell, D.T., Goriely, A., Hotaling, J.M., Cairns, B.R., 2018. The adult human testis transcriptional cell atlas. Cell Res 28, 1141–1157. https://doi.org/10.1038/s41422-018-0099-2.

Hao, Y., Li, W., Wang, Hui, Zhang, J., Wang, Haoyu, Dong, J., Yao, B., Xu, X., Zhao, L., Peng, R., 2022. Microwave radiation induces neuronal autophagy through miR-30a-5p/AMPKα2 signal pathway. Biosci. Rep. 42. https://doi.org/10.1042/BSR20212584.

Hao, Y., Liu, W., Liu, Yujie, Liu, Ying, Xu, Z., Ye, Y., Zhou, H., Deng, H., Zuo, H., Yang, H., Li, Y., 2023. Effects of nonthermal radiofrequency stimulation on neuronal activity and neural circuit in mice. Adv. Sci. 10, e2205988. https://doi.org/10.1002/advs.202205988.

Hasan, I., Rubayet Jahan, M., Nabiul Islam, M., Rafiqul Islam, M., 2022. Effect of 2400 MHz mobile phone radiation exposure on the behavior and hippocampus morphology in Swiss mouse model. Saudi J. Biol. Sci. 29, 102–110. https://doi.org/10.1016/j.sjbs.2021.08.063.

He, X., Li, Y., Dai, M.-S., Sun, X.-X., 2016. Ribosomal protein L4 is a novel regulator of the MDM2-p53 loop. Oncotarget 7, 16217–16226. https://doi.org/10.18632/oncotarget.7479.

Hermann, B.P., Cheng, K., Singh, A., Roa-De La Cruz, L., Mutoji, K.N., Chen, I.-C., Gildersleeve, H., Lehle, J.D., Mayo, M., Westernströer, B., Law, N.C., Oatley, M.J., Velte, E.K., Niedenberger, B.A., Fritze, D., Silber, S., Geyer, C.B., Oatley, J.M., McCarrey, J.R., 2018. The Mammalian Spermatogenesis Single-Cell Transcriptome, from Spermatogonial Stem Cells to Spermatids. e8 Cell Rep. 25, 1650–1667. https://doi.org/10.1016/j.celrep.2018.10.026.

Houston, B.J., Nixon, B., King, B.V., De Iuliis, G.N., Aitken, R.J., 2016. The effects of radiofrequency electromagnetic radiation on sperm function. Reproduction 152, R263–R276. https://doi.org/10.1530/REP-16-0126.

Jaffar, F.H.F., Osman, K., Ismail, N.H., Chin, K.-Y., Ibrahim, S.F., 2019. Adverse effects of Wi-Fi radiation on male reproductive system: a systematic review. Tohoku J. Exp. Med. 248, 169–179. https://doi.org/10.1620/tjem.248.169.

Jin, S., Guerrero-Juarez, C.F., Zhang, L., Chang, I., Ramos, R., Kuan, C.-H., Myung, P., Plikus, M.V., Nie, Q., 2021. Inference and analysis of cell-cell communication using CellChat. Nat. Commun. 12, 1088. https://doi.org/10.1038/s41467-021-21246-9.

Jones, R., James, P.S., Oxley, D., Coadwell, J., Suzuki-Toyota, F., Howes, E.A., 2008. The equatorial subsegment in mammalian spermatozoa is enriched in tyrosine phosphorylated proteins. Biol. Reprod. 79, 421–431. https://doi.org/10.1095/biolreprod.107.067314.

Korfanty, J., Toma, A., Wojtas, A., Rusin, A., Vydra, N., Widlak, W., 2012. Identification of a new mouse sperm acrosome-associated protein. Reproduction 143, 749–757. https://doi.org/10.1530/REP-11-0270.

L, O., Ri, M., Ng, W., Dm, R., 1994. Testosterone promotes the conversion of round spermatids between stages VII and VIII of the rat spermatogenic cycle. Endocrinology 135. https://doi.org/10.1210/endo.135.6.7988449.

L, O., Ri, M., Ng, W., Dm, de, K., Dm, R., 1996. Testosterone withdrawal promotes stage-specific detachment of round spermatids from the rat seminiferous epithelium. Biol. Reprod. 55. https://doi.org/10.1095/biolreprod55.4.895.

La, H., Yoo, H., Lee, E.J., Thang, N.X., Choi, H.J., Oh, J., Park, J.H., Hong, K., 2021. Insights from the applications of single-cell transcriptomic analysis in germ cell development and reproductive medicine. Int. J. Mol. Sci. 22. https://doi.org/10.3390/ijms22020823.

Li, H., Liang, Z., Yang, J., Wang, D., Wang, H., Zhu, M., Geng, B., Xu, E.Y., 2019. DAZL is a master translational regulator of murine spermatogenesis. Natl. Sci. Rev. 6, 455–468. https://doi.org/10.1093/nsr/nwy163.

Liu, L., Deng, H., Tang, X., Lu, Y., Zhou, J., Wang, X., Zhao, Y., Huang, B., Shi, Y., 2021. Specific electromagnetic radiation in the wireless signal range increases wakefulness in mice. Proc. Natl. Acad. Sci. USA 118. https://doi.org/10.1073/pnas.2105838118.

Liu, Y., Li, W., Zhou, S., Cui, M., Zhang, L., 2024. Pan-cancer analysis of the prognostic and immunological role of RPL4. Heliyon 10, e34461. https://doi.org/10.1016/j.heliyon.2024.e34461.

Lukassen, S., Bosch, E., Ekici, A.B., Winterpacht, A., 2018. Characterization of germ cell differentiation in the male mouse through single-cell RNA sequencing. Sci. Rep. 8, 6521. https://doi.org/10.1038/s41598-018-24725-0.

Maremanda, K.P., Khan, S., Jena, G.B., 2016. Role of zinc supplementation in testicular and epididymal damages in diabetic rat: involvement of Nrf2, SOD1, and GPX5. Biol. Trace Elem. Res 173, 452–464. https://doi.org/10.1007/s12011-016-0674-7.

Men, J., Zhang, L., Peng, R., Li, Y., Li, M., Wang, Hui, Zhao, L., Zhang, J., Wang, Haoyu, Xu, X., Dong, J., Wang, J., Yao, B., Guo, J., 2023. Metformin ameliorates 2.856 GHz microwave- radiation-induced reproductive impairments in male rats via inhibition of oxidative stress and apoptosis. Int. J. Mol. Sci. 24. https://doi.org/10.3390/ijms241512250.

Nguyen, E.B., Westmuckett, A.D., Moore, K.L., 2014. SPACA7 is a novel male germ cell-specific protein localized to the sperm acrosome that is involved in fertilization in mice. Biol. Reprod. 90, 16. https://doi.org/10.1095/biolreprod.113.111831.

Pacchierotti, F., Ardoino, L., Benassi, B., Consales, C., Cordelli, E., Eleuteri, P., Marino, C., Sciortino, M., Brinkworth, M.H., Chen, G., McNamee, J.P., Wood, A.W., Hooijmans, C.R., de Vries, R.B.M., 2021. Effects of radiofrequency electromagnetic field (RF-EMF) exposure on male fertility and pregnancy and birth outcomes: Protocols for a systematic review of experimental studies in non-human mammals and in human sperm exposed in vitro. Environ. Int 157, 106806. https://doi.org/10.1016/j.envint.2021.106806.

Peleg, M., Berry, E.M., Deitch, M., Nativ, O., Richter, E., 2023. On radar and radio exposure and cancer in the military setting. Environ. Res 216, 114610. https://doi.org/10.1016/j.envres.2022.114610.

Qamar, I., Park, E., Gong, E.Y., Lee, H.J., Lee, K., 2009. ARR19 (androgen receptor corepressor of 19 kDa), an antisteroidogenic factor, is regulated by GATA-1 in testicular Leydig cells. J. Biol. Chem. 284, 18021–18032. https://doi.org/10.1074/jbc.M900896200.

Raburn, D.J., Hamil, K.G., Tsuruta, J.K., O'Brien, D.A., Hall, S.H., 1995. Stage-specific expression of B cell translocation gene 1 in rat testis. Endocrinology 136, 5769–5777. https://doi.org/10.1210/endo.136.12.7588335.

Sato, T., Sako, Y., Sho, M., Momohara, M., Suico, M.A., Shuto, T., Nishitoh, H., Okiyoneda, T., Kokame, K., Kaneko, M., Taura, M., Miyata, M., Chosa, K., Koga, T., Morino-Koga, S., Wada, I., Kai, H., 2012. STT3B-dependent posttranslational N-glycosylation as a surveillance system for secretory protein. Mol. Cell 47, 99–110. https://doi.org/10.1016/j.molcel.2012.04.015.

Schiavi-Ehrenhaus, L.J., Romarowski, A., Jablonski, M., Krapf, D., Luque, G.M., Buffone, M.G., 2022. The early molecular events leading to COFILIN phosphorylation during mouse sperm capacitation are essential for acrosomal exocytosis. J. Biol. Chem. 298, 101988. https://doi.org/10.1016/j.jbc.2022.101988.

Shami, A.N., Zheng, X., Munyoki, S.K., Ma, Q., Manske, G.L., Green, C.D., Sukhwani, M., Orwig, K.E., Li, J.Z., Hammoud, S.S., 2020. Single-cell RNA sequencing of human, macaque, and mouse testes uncovers conserved and divergent features of mammalian spermatogenesis. Dev. Cell 54, 529–547.e12. https://doi.org/10.1016/j.devcel.2020.05.010.

Sharma, S., Hanukoglu, A., Hanukoglu, I., 2018. Localization of epithelial sodium channel (ENaC) and CFTR in the germinal epithelium of the testis, Sertoli cells, and spermatozoa. J. Mol. Histol. 49, 195–208. https://doi.org/10.1007/s10735-018-9759-2.

Shokri, S., Soltani, A., Kazemi, M., Sardari, D., Mofrad, F.B., 2015. Effects of Wi-Fi (2.45 GHz) exposure on apoptosis, sperm parameters and testicular histomorphometry in rats: a time course study. Cell J. 17, 322–331. https://doi.org/10.22074/cellj.2016.3740.

Subramanian, A., Tamayo, P., Mootha, V.K., Mukherjee, S., Ebert, B.L., Gillette, M.A., Paulovich, A., Pomeroy, S.L., Golub, T.R., Lander, E.S., Mesirov, J.P., 2005. Gene set enrichment analysis: a knowledge-based approach for interpreting genome-wide expression profiles. Proc. Natl. Acad. Sci. USA 102, 15545–15550. https://doi.org/10.1073/pnas.0506580102.

Stuart, T., Butler, A., Hoffman, P., Hafemeister, C., Papalexi, E., Mauck, W.M., Hao, Y., Stoeckius, M., Smibert, P., Satija, R., 2005. Comprehensive Integration of Single-Cell Data. Cell 177, 1888–1902. https://doi.org/10.1016/j.cell.2019.05.031 e21.

Tan, K., Song, H.W., Wilkinson, M.F., 2020. Single-cell RNAseq analysis of testicular germ and somatic cell development during the perinatal period. Development 147. https://doi.org/10.1242/dev.183251.

Tumkaya, L., Kalkan, Y., Bas, O., Yilmaz, A., 2016. Mobile phone radiation during pubertal development has no effect on testicular histology in rats. Toxicol. Ind. Health 32, 328–336. https://doi.org/10.1177/0748233713500820.

Van Damme, T., Gardeitchik, T., Mohamed, M., Guerrero-Castillo, S., Freisinger, P., Guillemyn, B., Kariminejad, A., Dalloyaux, D., van Kraaij, S., Lefeber, D.J., Syx, D., Steyaert, W., De Rycke, R., Hoischen, A., Kamsteeg, E.J., Wong, S.Y., van

Scherpenzeel, M., Jamali, P., Brandt, U., Nijtmans, L., Korenke, G.C., Chung, B.H.Y., Mak, C.C.Y., Hausser, I., Kornak, U., Fischer-Zirnsak, B., Strom, T.M., Meitinger, T., Alanay, Y., Utine, G.E., Leung, P.K.C., Ghaderi-Sohi, S., Coucke, P., Symoens, S., De Paepe, A., Thiel, C., Haack, T.B., Malfait, F., Morava, E., Callewaert, B., Wevers, R.A., 2017. Mutations in ATP6V1E1 or ATP6V1A cause autosomal-recessive Cutis Laxa. Am. J. Hum. Genet 100, 216–227. https://doi.org/10.1016/j.ajhg.2016.12.010.

Verbeek, J., Oftedal, G., Feychting, M., van Rongen, E., Rosaria Scarfì, M., Mann, S., Wong, R., van Deventer, E., 2021. Prioritizing health outcomes when assessing the effects of exposure to radiofrequency electromagnetic fields: a survey among experts. Environ. Int. 146, 106300. https://doi.org/10.1016/j.envint.2020.106300.

Vornoli, A., Falcioni, L., Mandrioli, D., Bua, L., Belpoggi, F., 2019. The contribution of in vivo mammalian studies to the knowledge of adverse effects of radiofrequency radiation on human health. Int J. Environ. Res Public Health 16. https://doi.org/10.3390/ijerph16183379.

Wang, H., Zhang, J., Hu, S.H., Tan, S.Z., Zhang, B., Zhou, H.M., Peng, R.Y., 2018. Real-time microwave exposure induces calcium efflux in primary hippocampal neurons and primary cardiomyocytes. Biomed. Environ. Sci. 31, 561–571. https://doi.org/10.3967/bes2018.077.

Yao, C., Dong, J., Ren, K., Sun, L., Wang, Hui, Zhang, J., Wang, Haoyu, Xu, X., Yao, B., Zhou, H., Zhao, L., Peng, R., 2023. Accumulative effects of multifrequency microwave exposure with 1.5 GHz and 2.8 GHz on the structures and functions of the immune system. Int. J. Environ. Res. Public Health 20. https://doi.org/10.3390/ijerph20064988.

Yu, G., Tang, Z., Chen, H., Chen, Z., Wang, L., Cao, H., Wang, Gang, Xing, J., Shen, H., Cheng, Q., Li, D., Wang, Guoren, Xiang, Y., Guan, Y., Zhu, Y., Liu, Z., Bai, Z., 2020. Long-term exposure to 4G smartphone radiofrequency electromagnetic radiation diminished male reproductive potential by directly disrupting Spock3-MMP2-BTB axis in the testes of adult rats. Sci. Total Environ. 698, 133860. https://doi.org/10.1016/j.scitotenv.2019.133860.

Yuan, W.B., Chen, H.Q., Li, J.Z., Zhou, S.M., Zeng, Y., Fan, J., Zhang, Z., Liu, J.Y., Cao, J., Liu, W.B., 2022. TET1 mediated male reproductive toxicity induced by Bisphenol A through Catsper-Ca (2+) signaling pathway. Environ. Pollut. 296, 118739. https://doi.org/10.1016/j.envpol.2021.118739.

Zhang, X., Huang, R., Zhou, Y., Zhou, W., Zeng, X., 2020. IP3R channels in male reproduction. Int. J. Mol. Sci. 21. https://doi.org/10.3390/ijms21239179.

Zhang, F.L., Ma, H.H., Dong, P.Y., Yuan, Z.N., Zhang, S.E., Zhao, A.H., Liu, H.Q., De Felici, M., Shen, W., Zhang, X.F., 2023. Aflatoxin B1 disrupts testicular development via the cell cycle-related Ras/PI3K/Akt signaling in mice and pig. Environ. Pollut. 329, 121729. https://doi.org/10.1016/j.envpol.2023.121729.

Zhao, L., Li, J., Hao, Y.H., Gao, Y.B., Wang, S.M., Zhang, J., Dong, J., Zhou, H.M., Liu, S. C., Peng, R.Y., 2017. Microwave-induced apoptosis and cytotoxicity of NK cells through ERK1/2 signaling. Biomed. Environ. Sci. 30, 323–332. https://doi.org/10.3967/bes2017.043.